Flow, Turbulence and Combustion **61:** 55–69, 1999.

Vibro-Acoustic Response of a Pipe Excited by a Turbulent Internal Flow

C. DURANT and G. ROBERT
Laboratoire de Mécanique des Fluides et d'Acoustique, UMR CNRS 5509, Ecole Centrale de Lyon, B.P. 163, 69131 Ecully Cedex, France

Abstract. This article presents an experimental study of the vibro-acoustic response of a pipe excited by a fully-developed turbulent air flow. First, the wall pressure field acting on the internal pipe wall is investigated. The power spectral density of the wall pressure fluctuations is analyzed after cancellation of contaminating background noise. The convection velocity and correlation lengths are calculated from measured cross-spectra, and the cross-spectra are expressed in Corcos model form. Second, the vibro-acoustic response of the pipe is analyzed by referring to the structural modes of the pipe.

Key words: pipe flow, wall pressure fluctuations, vibro-acoustic.

Abbreviations: PSD – power spectral density; RMS – root mean square.

1. Introduction

Flow-induced vibration and noise phenomena are of importance in several engineering problems. For example, in high speed transport technology, where structures are both lightweight and flexible, the action of the pressure fluctuations provides the driving force to excite surface vibrations and produce acoustic radiation.

The analysis of these phenomena is complex because they involve fluid mechanics, structural mechanics and acoustic radiation. First, it is necessary to have information on the statistical properties of the random wall pressure field which acts on the structure. Second, from the modelization of these properties and the motion equation of the structure, the vibration response is calculated. Third, the acoustic radiation is deduced from the vibration of the structure.

Considering the complexity of the problem, only some simple configurations have been studied. Some studies have been interested in flat plates excited by a turbulent boundary layer [1–3]. The case of a pipe excited by a fully-developed turbulent flow has also been investigated [4, 5]. The general aim of our experimental study is to provide an extensive databank characterizing this last configuration in order to make comparisons with future numerical predictions. To complete this databank, measurements of the internal wall pressure field generated by the flow, the vibration response and the external acoustic field are required.

For this experimental study, an air flow facility was designed and constructed to generate fully-developed turbulent flow in a 10 m long, 125 mm diameter smooth-walled pipe for Reynolds numbers $U_0 D/\nu$ ranging from 5.3×10^5 to 12.5×10^5, where U_0 is the centerline flow velocity, D the pipe diameter and ν the kinematic viscosity.

The object of this paper is to describe the experiments and results obtained by measuring the wall pressure field and the vibro-acoustic response of the pipe. First, the PSD and cross-spectral density of the wall pressure field in the streamwise and spanwise directions are presented. The PSD is analyzed after cancellation of any contaminating acoustic component. The convection velocity and correlation lengths are calculated from measured cross-spectra to complete a Corcos model [6] for the cross-spectrum of the turbulent wall pressure fluctuations. Second, the structural modes of the pipe test section are determined from a modal analysis. Third, the vibro-acoustic response is analyzed by referring to the structural modes.

2. Experimental Arrangement

Measurements were made in the wind tunnel of the Acoustic Center of Ecole Centrale de Lyon. The tunnel was specially designed to minimize acoustic contamination by upstream machinery and ambient noise. The primary air is first propelled to a slow speed by a centrifugal blower located in a special room, this room is isolated from the rest of the building for vibration reasons. Acoustic mufflers are situated both upstream and downstream of the blower in order to eliminate background noise. Then the air passes through an acceleration section made up of a honeycomb section, two sections of screens and a contraction with an area ratio of four. Finally, the air arrives in the last assembly, which is inside a large anechoic chamber. This last assembly, shown schematically in Figure 1, was made from interchangeable sections of steel tubing with an internal diameter of 125 mm, a wall thickness of 7.5 mm and an overall length of about 10 m. The bores of the various pipe sections were accurately matched, The test section was mounted 5 m ($\simeq$ 40 pipe diameters) downstream of the pipe entrance to achieve homogeneity and stationarity for the flow in the region of the test section.

The wall acceleration and the external acoustic pressure were measured for a 50 cm long and 0.5 mm wall thickness test section. The acceleration measurements were made with very light Bruël and Kjaër 4374 (0.65 gr) piezoelectric accelerometers located on several points on the wall of the test section. The external acoustic pressure was measured with Bruël and Kjaër 4135 (6.35 mm diameter) microphones at distances from the pipe wall ranging from 5 mm to 25 cm.

It was assumed that the vibrations of the test section did not modify the turbulent wall pressure field so that the statistical properties of the wall pressure were measured on the surface of a rigid section (7.5 mm thickness). This assumption was verified by comparing the RMS value of the displacement of the test section

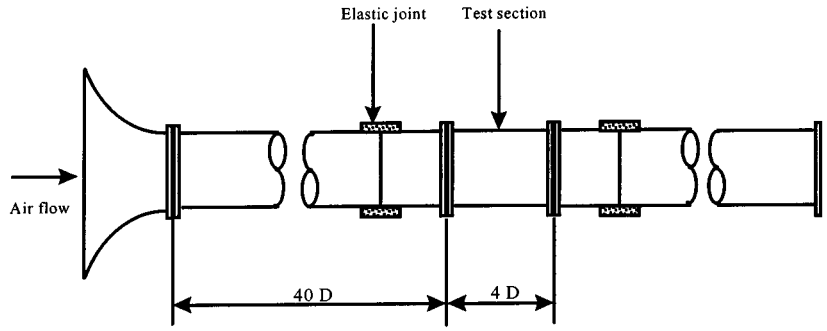

Figure 1. Pipe rig facility.

$((\overline{w^2})^{1/2})$ with respect to the laminar sublayer thickness of the flow. The laminar sublayer thickness was estimated by Schlichting [7]:

$$\delta_1 \simeq 5\frac{\nu}{U_f}, \tag{1}$$

where U_f is the friction velocity. For instance, for $U_0 = 140$ m/s, it was found that $(\overline{w^2})^{1/2} \simeq 0.2$ μm and $\delta_1 \simeq 12.5$ μm. The turbulent pressure sources are actually located beyond the laminar sublayer and as the RMS value of the displacement was found to be much lower than the laminar sublayer thickness, we concluded that the vibrations of the test section did not influence the turbulent wall pressure field.

The wall pressure measurements were made with 10 flush-mounted Bruël and Kjaër 4135 (6.35 mm diameter) microphones. By referring to the assumption of the separation of the spatial variables for the cross-spectra model [6], two series of measurements were made. First, the ten microphones were located along a line in the longitudinal direction; intervals varied from 8 mm to 242 mm with respect to the reference microphone. Next, the ten microphones were located on a circumference with angular separations varying from 8 to 160°.

The centerline velocity of the flow inside the pipe varied up to 140 m/s. Flow velocity measurements were made with a Dantec 55P11 hot-wire probe. The probe support was guided in the direction transverse to the flow. By translating the probe to various known locations along the pipe diameter, the velocity profile was recorded.

All measurements (velocity profile, wall pressure, acceleration response and acoustic pressure) were made for five centerline reference velocities: 60, 80, 100, 120 and 140 m/s.

Pressure signals were processed by an HP 3566A/67A analyzer (16 tracks, 12.8 kHz band width). The data were averaged over 1000 samples, so that random errors in the PSD of wall pressure fluctuations were on the order of 3% or 0.25 dB [8].

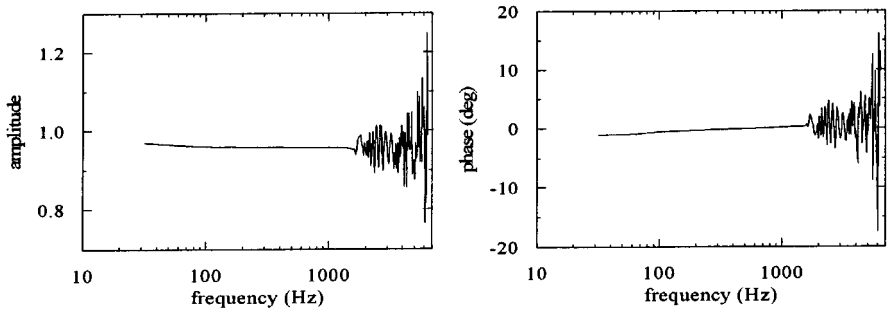

Figure 2. Amplitude and phase of transfer function.

3. Calibration Technique

The usual technique employed in measuring the sensitivities of the Bruël and Kjaër microphones consists of using an acoustic calibrator. The sound pressure level of the calibrator is 94 dB (ref. 2×10^{-5} Pa) at a frequency of 1 kHz. The sensitivity is deduced by measuring the output voltage given by the microphone when subjected to this level.

This technique presents two limitations. First, the sensitivity is known at only one frequency (1 kHz). Second, it does not give any information about the phase difference responses between the microphones. So, despite the high quality of the Bruël and Kjaër microphones, another technique was developed to calibrate the array of microphones. Note that the phase calibration is especially important because the convection velocity depends directly on the phase of the cross-spectra measured between microphones (see Section 4.2).

The technique used the pipe like a natural sound waveguide. Under the cutoff frequency ($\simeq$ 1.6 kHz), only plane, axially symmetric waves propagated, so that the array of microphones was subjected to a known acoustic excitation. By measuring the transfer functions between microphones, the sensitivities and the phase responses were deduced for each microphone. Physically, an acoustic source was placed at the downstream end of the pipe. To avoid reflexion of the waves at the upstream end, the source produced a burst of white noise, and the data acquisition was synchronized with the passage of the burst over the array of microphones. The simplest configuration of calibration was the circumferential implantation of the microphones. In this case, no additional phase difference was introduced by the propagation of the wave, and the phase of the transfer function directly gave the phase response between paired microphones. Figure 2 shows a typical transfer function observed between two microphones located on a same circumference. The amplitude of the transfer function actually represents the ratio between the sensitivities of the two microphones. The interpretation of results is limited to the frequency band [0, 1.6 kHz]. In this range, the flat line indicates a constant sensitivity for the two microphones. Thus, the sensitivity measured at 1 kHz by the

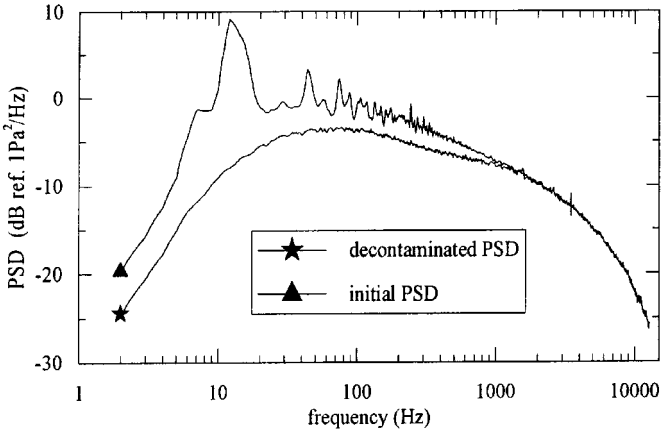

Figure 3. Power spectral densities at $U_0 = 100$ m/s.

acoustic calibrator is valid over the frequency band investigated. The phase shows a negligible shift, so that the two microphones agreed in phase.

The presented calibration technique permitted us to verify that the microphones functioned properly. Though the investigation was limited to the cutoff frequency of the pipe, the measured characteristics of the microphones were extended over the entire frequency band [0, 12.8 kHz] knowing the high performances of the Bruël and Kjaër microphones.

4. Results and Discussions

4.1. Power spectral density of the wall pressure fluctuations

To confirm that the turbulent flow in the pipe test section was fully-developed, the mean flow velocity profile was compared to the empirical distribution law proposed by Schlichting [7]. Though not shown, the good agreement between experimental results and empirical law ensured that the flow was fully developed in the pipe test section. Moreover, similarity observed between the PSD obtained from the different microphones ensures that the homogeneity hypothesis is verified for the statistical properties of the wall pressure in the test section.

Figure 3 shows the PSD of the wall pressure fluctuations recorded at $U_0 = 100$ m/s. The PSD covers a wide band but two frequency ranges are of special interest. In the low-frequency range, some peaks appear as observed by other investigators. These peaks come from acoustic modes of the pipe which are excited both by the noise produced by the turbulence inside the pipe and the background noise of the facility. Some papers [9, 10] have reported signal processing methods to cancel this acoustic component from the PSD of the wall pressure fluctuations. These methods are based on the principle that the acoustic field is more coherent than the turbulence in the spanwise direction. The method described in [9] was applied here

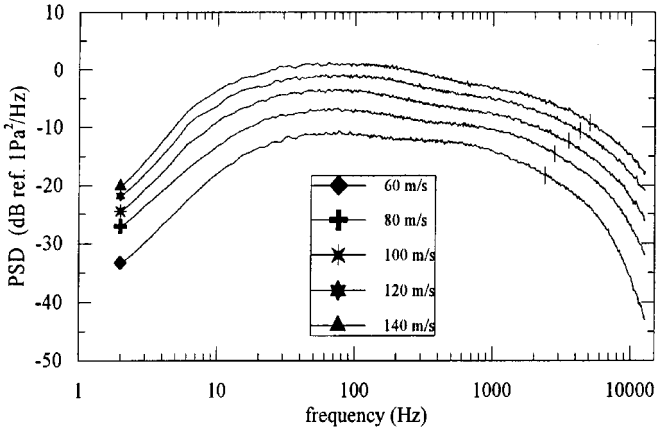

Figure 4. Decontaminated power spectral densities at 60, 80, 100, 120 and 140 m/s.

and the decontaminated PSD is presented in Figure 3. In the low-frequency range, the peaks are removed while the two PSD collapse at higher frequencies because no contamination exists. Therefore, it can be seen that the PSD of the turbulent wall pressure fluctuations increases slightly with frequency in the low-frequency range, then remains nearly constant and decreases at higher frequencies.

In the high-frequency range, the decrease of the PSD is accentuated by the lack of resolution of the microphone. To account for this lack of resolution, Corcos [11] proposed a correction factor for the PSD as a function of $\omega r/U_c$, where ω is the angular frequency, r the microphone radius and U_c the convection velocity. In Figure 3, the dash indicates the frequency limit beyond which the Corcos correction is greater than 3 dB.

Figure 4 presents the evolution of the decontaminated PSD as a function of the centerline velocity. When the centerline velocity increases, the spectral levels increase, and the decreasing part of the PSD is rejected in the range of higher frequencies. For each velocity, the dash indicates the frequency limit for a Corcos correction of 3 dB.

4.2. Cross-spectral features of the fluctuating pressure field

The cross-spectrum of the fluctuating pressure field $S_{pp}(\xi, \eta, \omega)$ was analyzed by using the model proposed by Corcos [6]:

$$S_{pp}(\xi, \eta, \omega) = S_{pp}(\omega) C(\xi, \eta, \omega) \exp(i\theta(\xi, \omega)), \tag{2}$$

where S_{pp} is the PSD of the wall pressure fluctuations and $\theta(\xi, \omega)$ the phase function which depends only on the longitudinal distance ξ because of the convection phenomena. The function $C(\xi, \eta, \omega)$ describes, as a function of frequency, the decay of the coherence of the pressure field as it is convected over a longitudinal

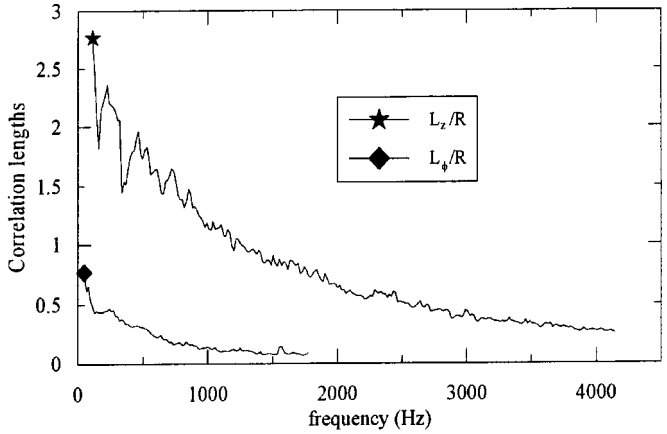

Figure 5. Correlation lengths nondimensionalized with pipe radius R at $U_0 = 100$ m/s.

distance ξ and a circumferential distance η. The hypothesis of separation of spatial variables permits one to write

$$C(\xi, \eta, \omega) = A(\xi, \omega)B(\eta, \omega). \tag{3}$$

The evolution of the coherence function $A(\xi, \omega)$ was deduced from the cross-spectrum $S_{pp}(\xi, 0, \omega)$ measured for several values of ξ owing to the longitudinal location of the microphones. Furthermore, the coherence function $B(\eta, \omega)$ was determined from the cross-spectrum $S_{pp}(0, \eta, \omega)$ measured in the circumferential direction. As a first approximation, the streamwise coherence function $A(\xi, \omega)$ and the spanwise coherence function $B(\eta, \omega)$ could be expressed in a decreasing exponential form with respect to ξ and η, respectively:

$$A(\xi, \omega) = \exp\left(\frac{-|\xi|}{L_z(\omega)}\right), \tag{4}$$

$$B(\eta, \omega) = \exp\left(\frac{-|\eta|}{L_\phi(\omega)}\right). \tag{5}$$

$L_z(\omega)$ and $L_\phi(\omega)$ are length scales that define the size of the correlation zone in the longitudinal and circumferential directions. Figure 5 shows the variation of these length scales as a function of frequency. The cross-spectral data were obtained without the cancellation of the acoustic component because the method proposed for the PSD [9] is not applicable for the cross-spectrum. Thus, at low frequency, the behavior of these length scales is rather perturbed because this zone is essentially governed by the acoustic component of the pressure field. At higher frequencies, the turbulent component dominates; $L_z(\omega)$ and $L_\phi(\omega)$ essentially describe the correlation length scales of the flow. Given the fact that coherence decreased much more rapidly in the transverse direction, $L_\phi(\omega)$ is clearly smaller than $L_z(\omega)$,

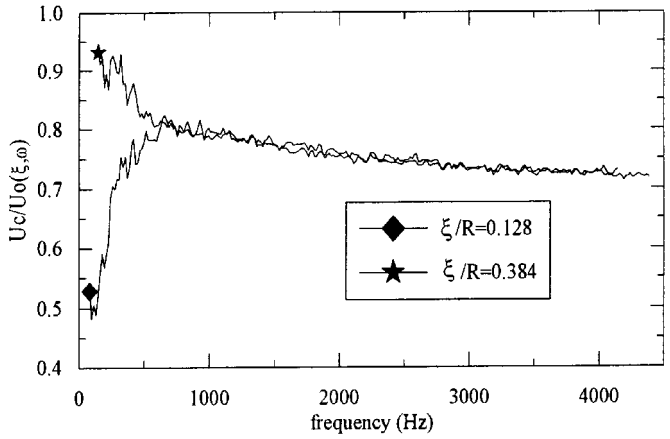

Figure 6. Evolution of the ratio U_c/U_0 at $U_0 = 100$ m/s.

which decreases continuously with frequency and thus expresses the fact that the small flow structures associated with high frequencies are convected over shorter distances than larger structures. In the mean, convection does not occur in the circumferential direction, thus the decrease of $L_\phi(\omega)$ is less pronounced.

A convection velocity $U_c(\xi, \omega)$ was obtained from the phase function of the cross-spectrum by

$$U_c(\xi, \omega) = \frac{-\omega\xi}{\theta(\xi, \omega)}. \tag{6}$$

Figure 6 presents the variation of the ratio $U_c(\xi, \omega)/U_0$ as a function of frequency for two fixed ξ. Two distinct zones appear in the variation of the ratio, as was the case with the PSD and the correlation lengths. In the low-frequency zone, the behavior of the ratio changes with ξ. This phenomenon can be explained by the presence of the acoustic component. Beyond this zone, the two curves collapse and the ratio is found to decrease slightly and continuously with frequency for all ξ. This decrease expresses the fact that the convection velocity of the large structures associated with the low frequencies is higher than the convection velocity associated with the small structures. That the ratio $U_c(\xi, \omega)/U_0$ was found to be between 0.7 and 0.8 is in good agreement with the literature.

In fact, the standard Corcos model does not directly involve $L_z(\omega)$ and $L_\phi(\omega)$ but expresses them by

$$L_z(\omega) = \frac{U_c(\xi, \omega)}{\alpha_z \omega}, \tag{7}$$

$$L_\phi(\omega) = \frac{U_c(\xi, \omega)}{\alpha_\phi \omega}. \tag{8}$$

This modelization is consistent with the dependence of the correlation zone on the centerline velocity and the frequency. Figure 7 shows the evolution of the

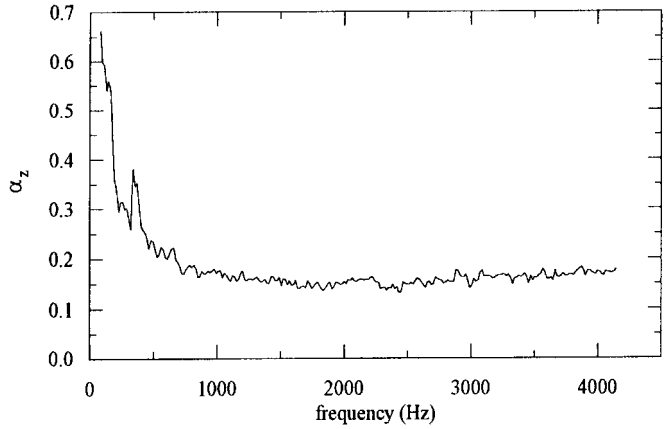

Figure 7. Evolution of the coefficient α_z at $U_0 = 100$ m/s.

coefficient α_z as a function of the frequency. The coefficient takes large values in the low-frequency range, then decreases, reaches a minimum and increases slightly again as the frequency rises. The large value for low frequencies ensures reasonable dimensions for $L_z(\omega)$ when $\omega \to 0$. The mean value of α_z appears to be a little bit larger than that reported by Robert [3] for a fully-developed turbulent boundary layer on a smooth plate ($\alpha_z \simeq 0.12$). Because of the rapid decrease of coherence in the circumferential direction, the coefficient α_ϕ can only be calculated in the low-frequency range where the acoustic component is preponderant. Thus, no specific information about α_ϕ is available until acoustic decontamination of the cross-spectral data can be achieved.

4.3. MODAL ANALYSIS OF THE PIPE TEST SECTION

The structural modes of the pipe test section were determined for two main reasons. On the one hand, the comparison between the measured and calculated structural modes permits us to confirm, for numerical predictions, that the pipe test section is correctly modeled by a clamped-clamped homogenous steel cylindrical shell. On the other hand, the knowledge of the modal frequencies is of interest in the interpretation of the vibro-acoustic response (see Section 4.4).

The modal analysis was made using a fixed accelerometer and a hammer for the excitation. The accelerometer was located near the upstream end of the pipe to "see" the whole of the structural modes. The pipe test section was excited by the hammer at 180 points located on the pipe by a mesh and the transfer functions between the excitation and the response of the accelerometer were recorded. Table I presents the results deduced from these 180 transfer functions. Each mode (n, m) is defined by its circumferential order n, its longitudinal order m, and its modal frequency f_{nm}. In Table I, the measured structural modes are compared with those calculated in [12] by a boundary integral equation method with standard mechan-

Table I. Measured and calculated structural modes of the pipe test section.

Modes number	Measured structural modes		Calculated structural modes	
	Order	Frequency (Hz)	Order	Frequency (Hz)
1	(3,1)	565	(3,1)	571
2	(4,1)	570	(4,1)	580
3	(5,1)	794	(5,1)	803
4	(2,1)	937	(4,2)	932
5	(4,2)	942	(2,1)	950
6	(5,2)	959	(5,2)	954
7	(6,1)	1131	(6,1)	1132
8	(6,2)	1207	(6,2)	1203
9	(3,2)	1301	(3,2)	1273
10	(5,3)	1311	(5,3)	1281
11	(6,3)	1390	(6,3)	1371

ical characteristics for steel ($E = 195$ GPa; $\nu = 0.33$; $\rho = 7850$ Kg/m^3). Quite good agreement is observed between the measured and calculated results. Up to 1400 Hz, the structural modes appear to be in the same order except for the fourth and fifth modes which are, however, very close. The relative error of the modal frequencies is less than 2% for all modes. Above 1400 Hz, the modal density is too great for correct modal identification. This comparison confirms that a clamped-clamped homogeneous steel cylindrical shell is a valid model to represent the pipe test section for future numerical predictions.

Moreover, the pipe test section was found to be lightly damped with a damping factor of about 4×10^{-4}. This damping factor was found to be approximately constant for all structural modes.

4.4. VIBRO-ACOUSTIC RESPONSE OF THE PIPE TEST SECTION

The acceleration response and the external acoustic pressure radiated from the pipe test section were measured at several locations for the five reference flow velocities. Figures 8 and 9 present the results for $U_0 = 100$ m/s. Figure 8 shows the PSD of the acceleration response measured at 10 cm from the upstream end of the pipe test section. Figure 9a shows the PSD of the acoustic pressure measured at the same location as the acceleration response but at a radial distance of 5 mm from the pipe wall. Figure 9b presents the PSD of the acoustic pressure at a radial distance of 25 cm.

Many distinct peaks appear in the PSD of the acceleration response. The first peaks are identified in Figure 8 and correspond to the structural modes of the pipe test section. As the excitation provided by the flow is wide-band, all the struc-

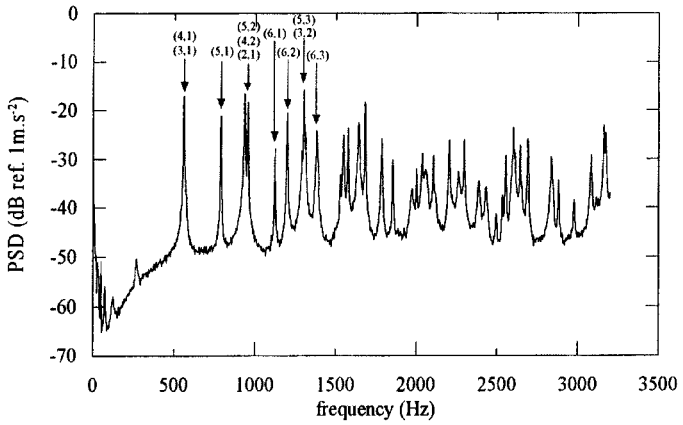

Figure 8. Power spectral density of the acceleration response at $U_0 = 100$ m/s.

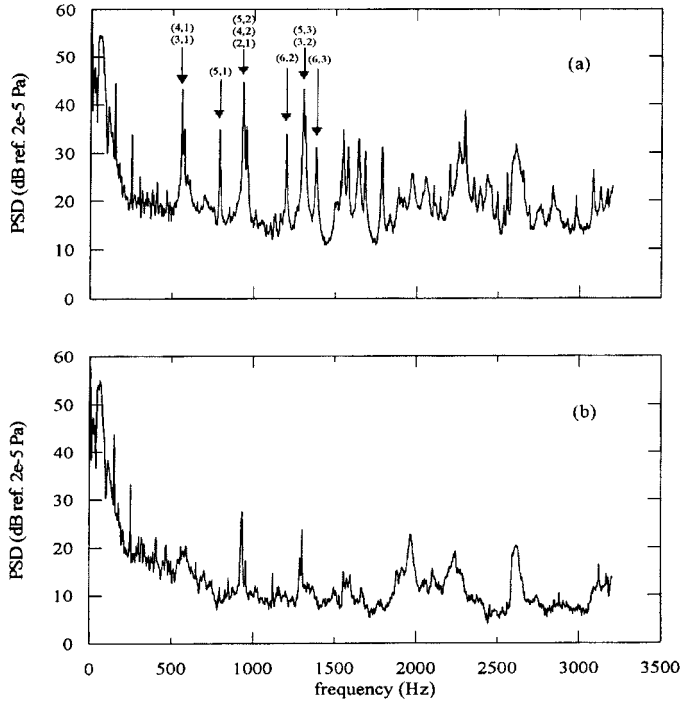

Figure 9. Power spectral density of the acoustic pressure at 5 mm (a) and 25 cm (b) from the pipe wall at $U_0 = 100$ m/s.

tural modes make a contribution to the PSD of the acceleration response. Under 1500 Hz, the modal density is weak and the peaks are well separated. As the pipe test section is lightly damped, these peaks are thin and present a large magnitude ($\simeq$ 30 dB).

The PSD of the acoustic pressure measured at both 5 mm and 25 cm show a low-frequency zone (under 200 Hz) dominated by the external background noise. Beyond this zone, the level of the acoustic pressure radiated from the pipe test section at 5 mm (Figure 9a) emerge from the background noise. Some peaks appear clearly in the PSD and can be associated with the structural modes. However, some structural modes do not make any contribution. For instance, the (6,1) mode does not appear in the PSD of acoustic pressure, though it was identified in the PSD of the acceleration response. Figure 9b shows that the acoustic pressure decreases rapidly with distance from the pipe wall. Indeed, only some modes emerge from the background noise. This phenomenon can be explained with regard to the characteristic frequencies of the pipe test section, i.e. the ring frequency f_r and the acoustic coincidence frequency f_c defined by

$$f_r = \frac{1}{\pi D}\sqrt{\frac{E}{\rho(1-\nu^2)}}, \tag{9}$$

$$f_c = \frac{c_o^2}{2\pi h}\sqrt{\frac{12\rho(1-\nu^2)}{E}}, \tag{10}$$

where h is the wall thickness, E is the Young modulus, ρ is the steel density, ν is the Poisson coefficient and c_o is the speed of sound. The ring frequency is found to be around 13.6 kHz and the coincidence frequency around 23.7 kHz. The radiation efficiency is an important parameter in the vibro-acoustic response of the pipe; it determines the external acoustic pressure level due to the pipe wall vibration. The ring-frequency range and the coincidence-frequency range are two regions where the radiation efficiency is maximum [13]. The frequency range studied for the vibro-acoustic response (under 3 kHz) is far away from these frequency ranges and the radiation efficiency is therefore very weak. Thus, it is consistent to observe an acoustic pressure level that is much lower than the pipe wall vibration level and that rapidly decreases with the distance from the pipe wall.

Figure 10 presents the RMS values of different quantities (wall pressure field, acceleration response and acoustic pressure) as a function of the centerline flow velocity. Each RMS value was calculated from the integration of the PSD over the frequency band [300, 3000 Hz]. The lower limit of integration was chosen to remove the background noise region observed in the PSD of the acoustic pressure. The upper limit of integration was fixed with regard to the loss of resolution of the microphone in the measurement of the PSD of the wall pressure field. Each RMS value was thus obtained from the general formula:

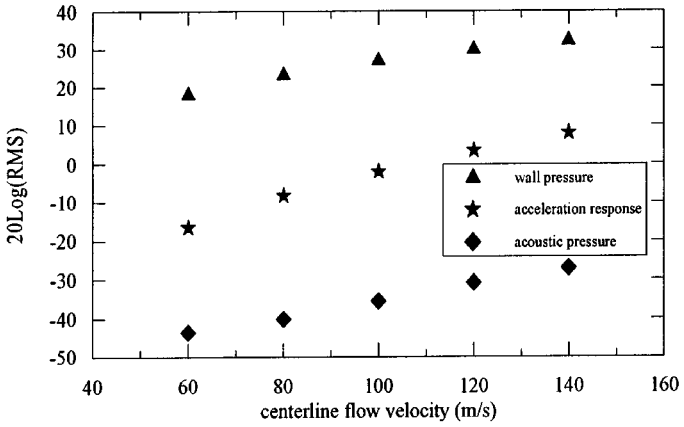

Figure 10. Evolution of the RMS value of the wall pressure field, the acceleration response and the acoustic pressure with the centerline velocity.

$$\mathrm{RMS} = \left[\int_{300}^{3000} \mathrm{PSD}(f)\,\mathrm{d}f \right]^{1/2} . \tag{11}$$

The evolutions of the RMS values are not completely linear and the slope decreases as the centerline velocity increases. For the wall pressure field, the RMS value grows with a slope of nearly 40 dB per decade, which corresponds to an evolution with the square of the centerline velocity. This was previously observed by other investigators [3, 4]. The RMS value of the acceleration response has a slope greater than the RMS value of the wall pressure field. This can be attributed to aerodynamic coincidences phenomena. The evolution of the RMS value of the acoustic pressure (measured at 5 mm) is identical to that of the RMS value of the wall pressure field.

5. Concluding Remarks

This investigation produced an extended database on the PSD and cross-spectra of the wall pressure fluctuations for a fully-developed turbulent pipe flow. The database was completed by the PSD of the acceleration response and external acoustic pressure radiated from a 50 cm long, 125 mm diameter and 0.5 mm wall thickness pipe test section. All these results were obtained for flow velocities ranging from 60 to 140 m/s.

In the low-frequency range, the PSD of the wall pressure fluctuation showed the presence of an acoustic component superimposed on the turbulence contribution. A signal processing method [9] was employed to cancel this component. The characteristic quantities of the flow, i.e., the convection velocity, the correlation lengths and the coefficient α_z were determined from the cross-spectral data. As no acoustic cancellation technique was used for the cross-spectra processing, the evolutions of these quantities were rather disturbed in the low-frequency range.

A new investigation will involve an acoustic cancellation technique to gain further information about the characteristics of the turbulent wall pressure field. After that, all quantities will be included in a Corcos model of the cross-spectrum:

$$S_{pp}(\xi, \eta, \omega) = S_{pp}(\omega) \exp\left(-\alpha_z \frac{\omega|\xi|}{U_c(\xi, \omega)}\right) \times \exp\left(-\alpha_\phi \frac{\omega|\eta|}{U_c(\xi, \omega)}\right) \exp\left(-i \frac{\omega\xi}{U_c(\xi, \omega)}\right). \quad (12)$$

The cross-spectrum is the statistical characteristic of the wall pressure field required for numerical predictions. Its knowledge can be extended to any flow velocity, other than reference velocities, by nondimensionalization of spectral data with appropriate scales of pressure, length and time. Some works [14, 15] have already demonstrated the effectiveness of particular scaling laws in order to collapse data.

The modal analysis confirmed that the pipe test section behaved as a real clamped-clamped homogeneous steel cylindrical shell. Therefore, all necessary information about the excitation and the structure are now available for inclusion in numerical predictions. The performances of these numerical predictions can thus be evaluated by comparison with the PSD of the acceleration response and the external acoustic pressure presented in Section 4.4.

References

1. Maestrello, M., Radiation from and panel response to a supersonic turbulent boundary layer. *Journal of Sound and Vibration* **10**(2) (1969) 261–295.
2. Davies, H.G., Sound from turbulent boundary layer excited panels. *Journal of the Acoustical Society of America* **49**(3) (1971) 878–889.
3. Robert, G., Modélisation et simulation du champ excitateur induit sur une structure par une couche limite turbulente. Thèse, Ecole Centrale de Lyon, France (1984).
4. Clinch, J.M., Measurements of the wall pressure field at the surface of a smooth-walled pipe containing turbulent water flow. *Journal of Sound and Vibration* **9**(3) (1968) 398–419.
5. Norton, M.P. and Bull, M.K., Mechanisms of the generation of external acoustic radiation from pipes due to internal flow disturbances. *Journal of Sound and Vibration* **94**(1) (1984) 105–146.
6. Corcos, G.M., The resolution of turbulent pressures at the wall of a boundary layer. *Journal of Sound and Vibration* **6**(1) (1967) 59–70.
7. Schlichting, H., *Boundary-Layer Theory*. McGraw-Hill, New York (1979).
8. Bendat, J.S. and Piersol, A.G., *Random Data: Analysis and Measurements Procedure*. Wiley and Sons, New York (1971).
9. Horne, M.P. and Handler, R.A., Note on the cancellation of contamining noise in the measurement of turbulent wall pressure fluctuations. *Experiments in Fluids* **12** (1991) 136–139.
10. Lauchle, G.C. and Daniels, M.A., Wall-pressure fluctuations in turbulent pipe flow. *Physics of Fluids A, Fluids Dynamics* **30**(10) (1987) 3019–3024.
11. Corcos, G.M., Resolution of pressures in turbulence. *Journal of the Acoustical Society of America* **35**(2) (1963) 192–199.
12. Durant, C., Filippi, P., Laulagnet, B., Mattéi, P.-O. and Robert, G., Réponse vibro-acoustique des structures excitées par des écoulements. In: *Colloque GDR Vibro-acoustique 1138*, Le Mans. Publication du LNA, No. 144 (1997) pp. 69–94.

13. Lesueur C., *Rayonnement Acoustique des Structures*. Eyrolles, Paris (1988) p. 171.
14. Farabee, T.M. and Casarella, M.J., Spectral features of wall pressure fluctuations beneath turbulent boundary layers. *Physics of Fluids A, Fluids Dynamics* **3**(10) (1991) 2410–2420.
15. Keith, W.L., Hurdis, D.A. and Abraham, B.M., A comparison of turbulent boundary layer wall-pressure spectra. *Journal of Fluids Engineering* **114** (1992) 338–347.